Supplementary information

Versatile nanoporous bimetallic phosphides towards electrochemical water splitting

Yongwen Tan,[a,b] Hao Wang,[b] Pan Liu,[a,b] Yuhao Shen,[b,c] Chun Cheng,[b] Akihiko Hirata,[b] Takeshi Fujita,[b] Zheng Tang,[c] Mingwei Chen,[a,b,d]*

[a] State Key Laboratory of Metal Matrix Composites, School of Materials Science and Engineering, Shanghai Jiao Tong University, Shanghai 200030, PR China

[b] WPI Advanced Institute for Materials Research, Tohoku University, Sendai 980-8577, Japan.

[c] Key Laboratory of Polar Materials and Devices, East China Normal University, Shanghai 200062, China

[d] CREST, JST, 4-1-8 Honcho Kawaguchi, Saitama 332-0012, Japan

*Correspondence to: mwchen@wpi-aimr.tohoku.ac.jp

Supplementary Methods, Figures, Table and Discussion

Methods

Preparation of precursor Co-Fe-P ribbons. Co-Fe-P alloy ingots were prepared by arc melting Co_2P, pure Co and pure Fe under an argon atmosphere. The Co:Fe:P atomic ratios were designed in a wide composition range to fabricate np-$(Co_{1-x}Fe_x)_2P$. A melt spinning technique was introduced to rapidly quench the re-melt the alloy ingots by the cold surface of a spinning copper roller to achieve a homogeneous nanocrystalline two-phase ribbons with the dimensions of ~1 mm wide and 20 μm thick. The grain sizes of the ribbons were tuned by changing the rotation rates of the

copper roller from 1,000 revolutions per minute (1 Krpm) to 5 Krpm. The ribbons were cut into thin plates with dimensions of 1 mm wide and 10 mm long for the fabrication of nanoporous $(Co_{1-x}Fe_x)_2P$ catalysts.

Fabrication of np-$(Co_{1-x}Fe_x)_2P$. The Co-Fe-P ribbons were electrochemically etched in 0.5 M H_2SO_4 solution in a standard three-electrode configuration with a Ag/AgCl electrode as the reference electrode and a graphite sheet as the counter electrode using an electrochemical workstation (lvium Technology). The selective phase dissolution process was controlled by etching time. The applied potential was determined by the measurements of the critical oxidation potentials of the BCC CoFe phase and the $(Co_{1-x}Fe_x)_2P$ compound. The np-$(Co_{1-x}Fe_x)_2P$ phosphides were obtained at a dealloying voltage of 0.03 V for 3000 s after the full dissolution of the BCC CoFe phase. The dealloyed samples were rinsed by deionized water for more than three times to remove the residual chemical substances within nanopore channels.

Structural characterization. XRD patterns of precursor Co-Fe-P ribbons and np-$(Co_{1-x}Fe_x)_2P$ phosphides were taken using a Rigaku Ultima X-ray diffractometer with Cu Ka radiation. Microstructure and chemical composition were inspected with a JEOL JIB-4600F SEM equipped with an Oxford energy dispersive X-ray spectroscopy. The HRTEM and STEM images were taken by a 200 kV JEOL JEM-2001F equipped with double spherical aberration (Cs) correctors for both the probe-forming and image-forming objective lenses. The chemical state and composition of the samples were characterized using X-ray photoelectron spectroscopy (XPS, AxlS-ULTRA-DLD) with Al Ka (mono) anode at energy of 150 W. Surface areas and pore

sizes of np-$(Co_{1-x}Fe_x)_2P$ were measured by the Brunauer–Emmett–Teller (BET) method and Barrett-Joyner- Hallender (BJH) method at 77.0 K using a BELSORP-mini II (BEL. JAPAN. INC). The horizontal axis was normalized with the vapor pressure of nitrogen (P_0) at 77.0 K (= 0.101 MPa). The samples were heated at 80°C under vacuum for 12 hours before the measurements. The mass of the sample were measured with an ultra-micro balance.

Electrochemical characterizations. The electrocatalytic activities of np-$(Co_{1-x}Fe_x)_2P$ were tested at room temperature. HER and OER tests were conducted in a three-electrode cell by using an electrochemical workstation (lvium Technology. Linear scan voltammetry was constructed out at a scan rate of 2 mV s^{-1} with an Ag/AgCl electrode as the reference electrode and a graphite sheet as the counter electrode. The electrolytes were 0.5 M H_2SO_4 and 1.0 M KOH made with deionized water and were continuously purged with high-purity Ar. The reference electrode was calibrated to reversible hydrogen potential (RHE) using platinum electrode for both working and counter electrodes in the same electrolyte, and converted to RHE according to the Nernst equation ($E_{RHE}=E_{Ag/AgCl}+ E^0_{Ag/AgCl} + 0.0591pH$). Overall water splitting is performed in a two-electrode system. One np-$(Co_{1-x}Fe_x)_2P$ ribbon (or IrO_2) electrode acts as the positive electrode for OER and the other np-$(Co_{1-x}Fe_x)_2P$ ribbon (or Pt/C) is used as the negative electrode for HER. All CV curves presented here were corrected for iR losses unless otherwise noted. The current densities are based on geometric areas. The Pt/C and IrO_2 inks were loaded on a glassy carbon electrode (surface area: 0.419 cm^2), the loading mass is 1.0 mg/cm^2.

DFT calculations. The spin-polarized density functional theory calculations were performed using a slab structural model by the Vienna *ab initio* simulation package (VASP) with the generalized gradient approximation (GGA). The plane wave pseudopotential with a cutoff energy at least 500.0 eV and a 8×8×1 Monkhorst-Pack k grid were adopted in the self-consistent convergence. By the structure relaxation the atomic geometries were fully optimized until the Hellmann-Feynman forces were less than 0.01 eV/Å. The hydrogen adsorption free energy　　was calculated as below：

—

where　　is the energy of a gas phase hydrogen molecule,　　is the zero-point energy difference between the adsorbed state of the system and the gas state, and is the entropy difference between the adsorbed state of the system and the gas phase standard state (300 K, 1 bar). As the contribution from the vibrational entropy of H in the adsorbed state is negligibly small, the entropy of hydrogen adsorption is defined as　　$\approx 1/2$　, where　　is the entropy of H_2 in the gas phase at the standard conditions. The Gibbs free energy with the overall corrections was taken as:　　.

Turnover frequency (TOF) calculations. The TOF values are calculated according to the following equation[1]:

$$TOF\ (H_2\ /s) = \frac{\#total\ hydrogen\ turnovers\ per\ geometric\ area}{\#active\ sites\ per\ geometric\ area}$$

The number of total hydrogen turnovers is calculated from the current density according to:

$$\#total\ hydrogen\ turnovers$$
$$= \left(j\frac{mA}{cm^2}\right)\left(\frac{1\ C\ s^{-1}}{1000\ mA}\right)\left(\frac{1\ mol\ e^-}{96485.3\ C}\right)\left(\frac{1\ mol\ H_2}{2mol\ e^-}\right)\left(\frac{6.022\ \times 10^{23}\ H_2 m}{1\ mol\ H_2}\right.$$

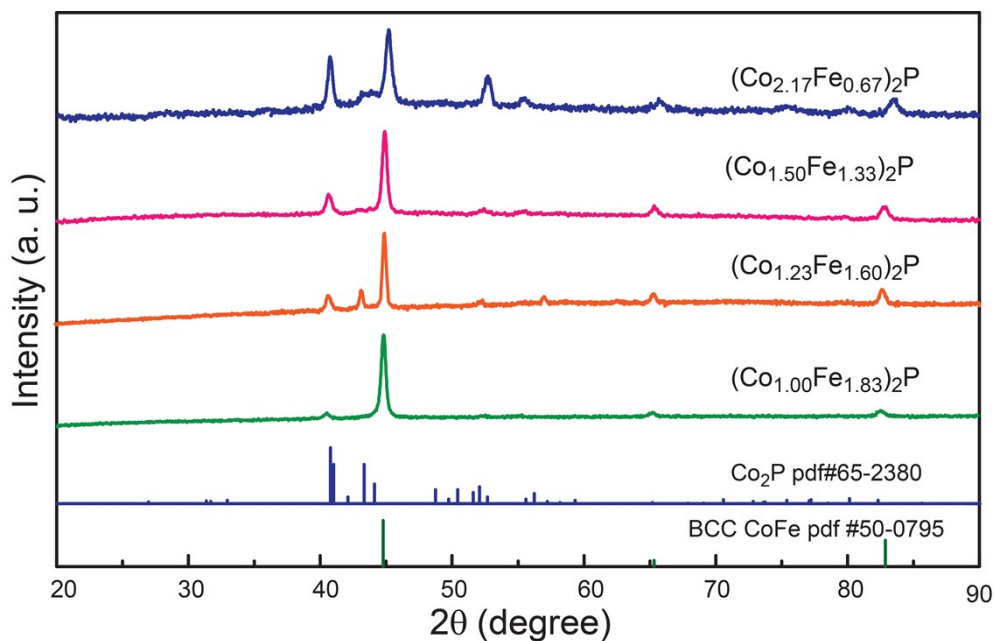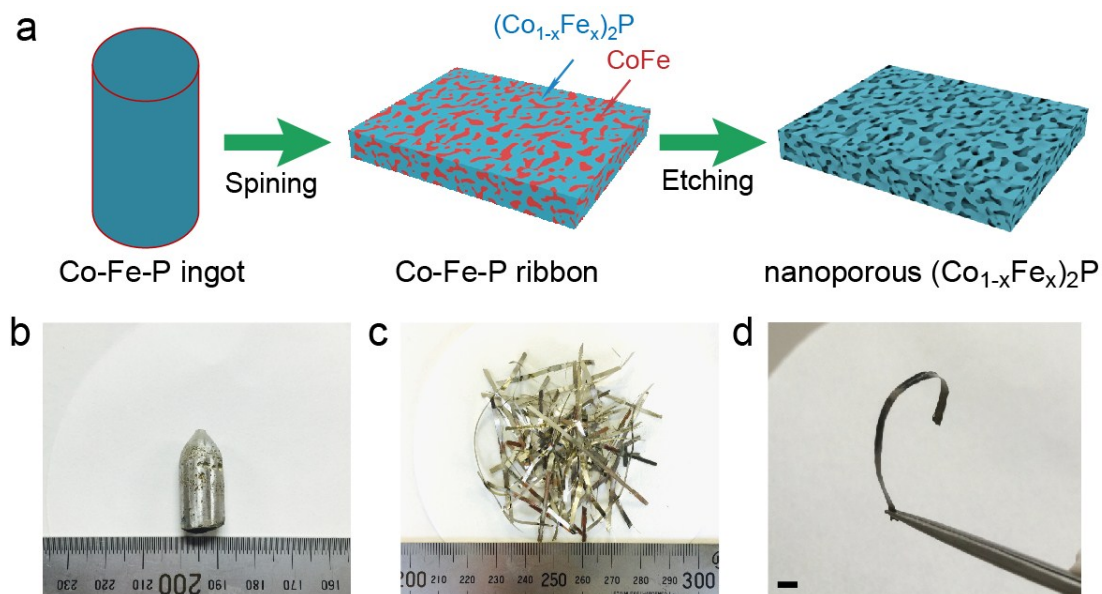$$= 3.12 \times 10^{15} \frac{H_2/s}{cm^2} \, per \, \frac{mA}{cm^2}$$

We can estimate the number of active sites as the total number of surface sites from the roughness factor together with the unit cell of orthorhombic $(Co_{1-x}Fe_x)_2P$. The surface sites (atoms cm^{-2}_{real}) is estimated by using the method suggested by Ref. 1:

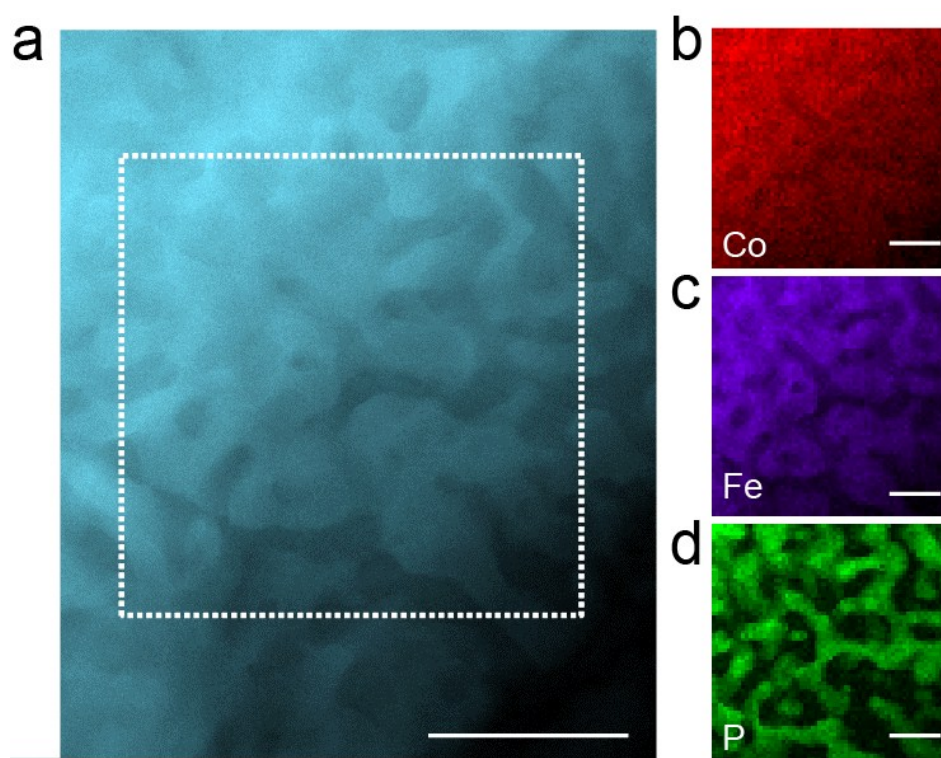*#Surface sites* $= 2.017 \times 10^{15}$ atoms cm^{-1}_{real}

Finally, the current density from the LSV polarization curves are converted into the TOF values at different operation potentials according to:

$$TOF = \frac{\left(3.12 \times 10^{15} \frac{H_2/s}{cm^2} \, per \, \frac{mA}{cm^2} \right) \times |j|}{(\#suface \; sites) \times (BET) \times (mass)}$$

For np-$(Co_{0.52}Fe_{0.48})_2P$ with 20 nm pore size, the loading mass is ~2.5 mg. Therefore, the TOF values were calculated to be: *TOF (0.05V vs RHE)*=0.009 H_2 s^{-1}, *TOF (0.1V vs RHE)*=0.1 H_2 s^{-1}..

Figure S1 (a) Schemical description of the fabrication process of free-standing nanoporous $(Co_{1-x}Fe_x)_2P$. **(b)** The optical photograph of a mother alloy ingot; **(c)** melt-spun ribbon precursors; and **(d)** an as-prepared nanoporous $(Co_{1-x}Fe_x)_2P$ ribbon. Scale bar: **(d)** 1 mm. The precursor ribbons contain BCC CoFe and orthorhombic $(Co_{1-x}Fe_x)_2P$ phases. After electrochemical leatching, the BCC CoFe phase is removed by selective phase dissolution. Finally, we can obtain the free-standing 3D nanoporous $(Co_{1-x}Fe_x)_2P$ with controllable Co/Fe ratios.

Figure S2 X-ray diffraction pattern of Co-Fe-P percursor alloys with different Co/Fe ratios.

Figure S3 TEM characterization of a rapidly-solidified Co-Fe-P precursor ribbons. (a) High-angle annular dark-field scanning TEM image of the rapidly-solidified alloy. The marked box is the selected region for EDS chemical analysis. (b-d) TEM EDS element mappings of the alloy taken from the marked region in (a). Scale bars: (a) 50 nm, (b-d) 25 nm.
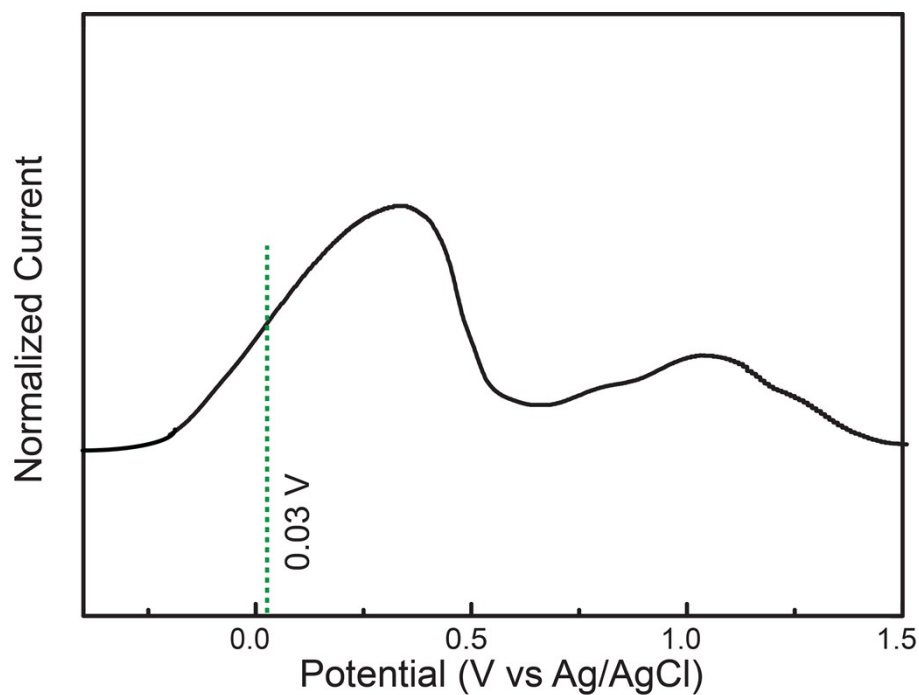
Figure S4 The linear sweep voltammetry (LSV) curve of a Co-Fe-P alloy in 0.5 M H_2SO_4. There are two distinct peaks corresponding to the oxidation (or dissolution) of the BCC CoFe and $(Co_{1-x}Fe_x)_2P$ phases, respectively. The critical dissolution potential of the CoFe phase is ~-0.25 V vs. Ag/AgCl while it is ~0.55 V for the dissolution of the phosphide phase. In this study we selected the corrosion potential of 0.03 V for the selective dissolution of the BCC CoFe phase at which the $(Co_{1-x}Fe_x)_2P$ phase is safe.
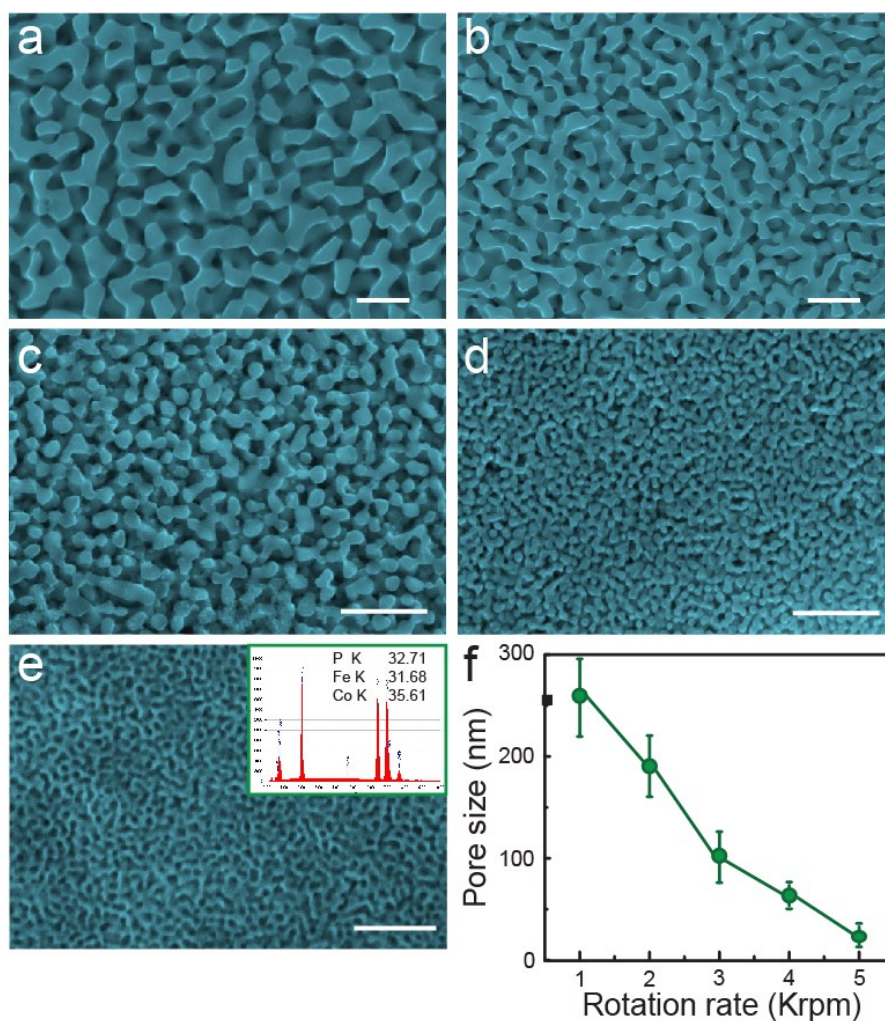
Figure S5 SEM images of np-(Co$_{0.52}$Fe$_{0.48}$)$_2$P with controllable pore sizes. The pore sizes were tailored by the cooling rates of melt spinning (1,000 revolutions per minute (Krpm) of the copper roller) from (a) 1 Krpm; (b) 2 Krpm; (c) 3 Krpm; (d) 4 Krpm, (e) 5 Krpm; Inset is EDS spectra showing the ratio of the Co, Fe and P elements. **(f)** Tunable pore sizes as a function of the rotation rates. The pore size can be tailored from ~20 to 260 nm from 5 to 1 Krpm. Scale bars: (a-d) 500 nm; (e) 200 nm.
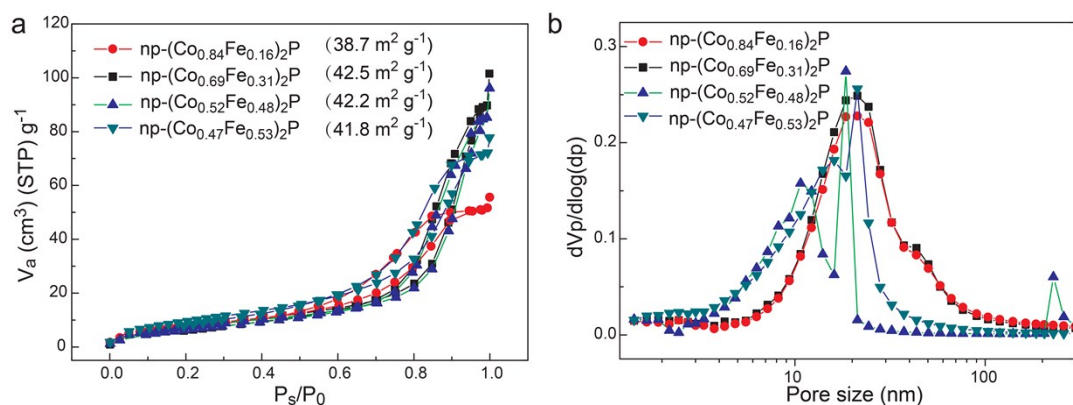
Figure S6 (a) N$_2$ adsorbing-desorbing isotherm curves of np-(Co$_{1-x}$Fe$_x$)$_2$P with different Co/Fe ratios. (b) The pore size distrubtion of as-prepared np-(Co$_{1-x}$Fe$_x$)$_2$P.
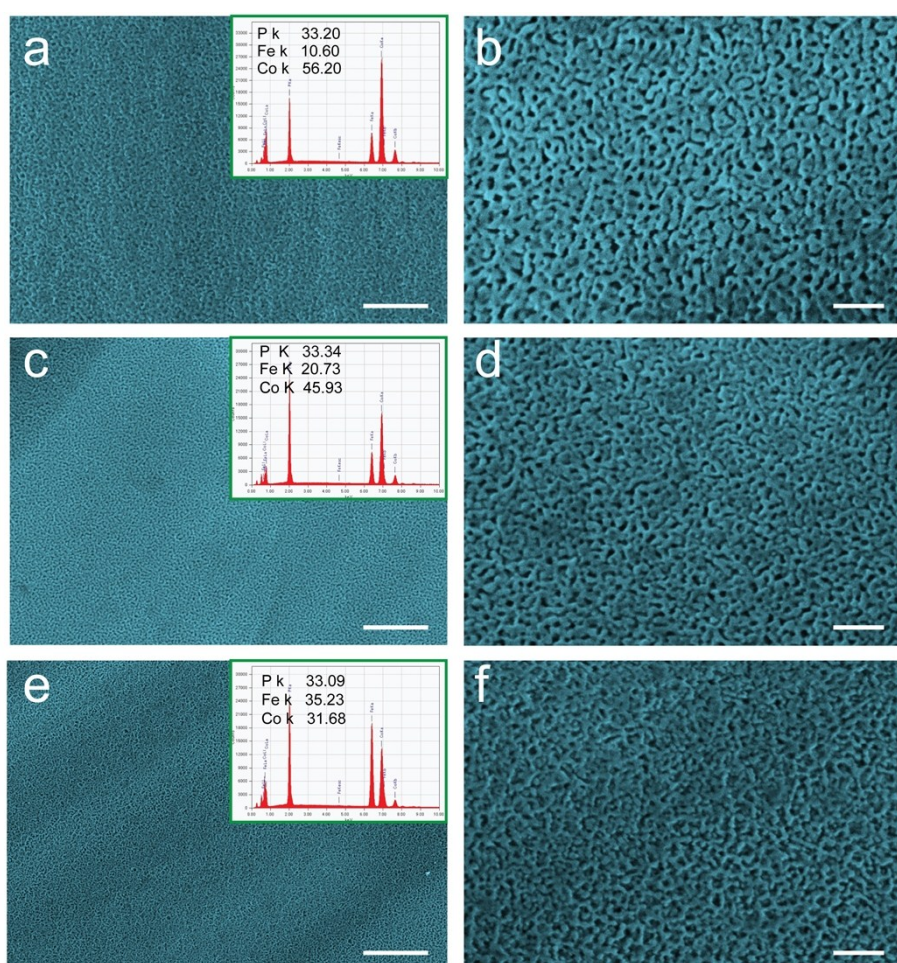

Figure S7 SEM images of np-(Co$_{1-x}$Fe$_x$)$_2$P with different Co/Fe compositions prepared by changing the Co/Fe ratios of precursor Co-Fe-P ribbons. (a, b) (Co$_{0.84}$Fe$_{0.16}$)$_2$P, (c, d) (Co$_{0.69}$Fe$_{0.31}$)$_2$P, and (e, f) (Co$_{0.47}$Fe$_{0.53}$)$_2$P. Insets are EDS spectra showing the compositions of the np-(Co$_{1-x}$Fe$_x$)$_2$P. (a), (c) and (e) the low magnification SEM images show a uniform nanoporous structure across the entire samples. Scale bars: (a), (c) and (e) 1 μm; (b), (d) and (f) 200 nm.
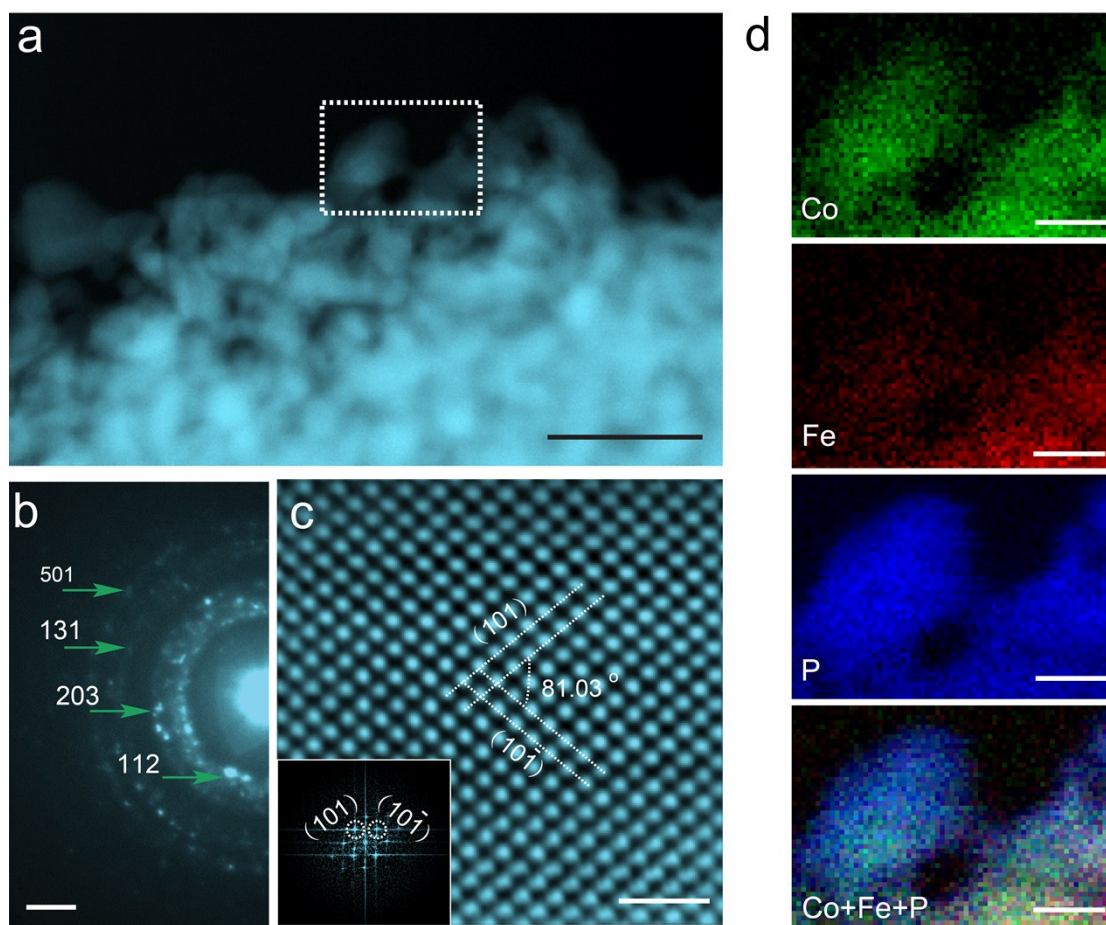
Figure S8 Structure ananlyses of nanoporous $(Co_{0.52}Fe_{0.48})_2P$. (a) High-angle annular dark-fied scanning transmission electron micrograph (HAADF-STEM) images of the nanoporous $(Co_{0.52}Fe_{0.48})_2P$. **(b)** Selected area electron diffraction (SAED) of np-$(Co_{0.52}Fe_{0.48})_2P$. **(c)** HRTEM images of lattice crystalline of np-$(Co_{0.52}Fe_{0.48})_2P$. **(d)** STEM-EELS element mappings of np-$(Co_{0.52}Fe_{0.48})_2P$ showing the uniform distribution of Co, Fe, and P in the nanoporous structure. Scale bars: (a) 50 nm; (b) 1/5 nm, (c) 1 nm, and (d) 20 nm.
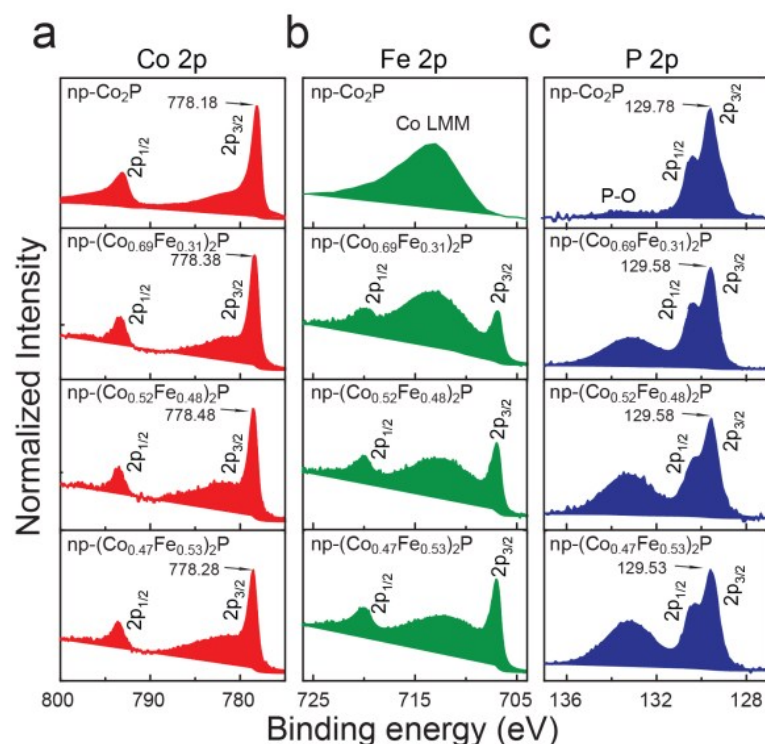
**Figure S9** XPS spectra of binary np-Co$_2$P and np-(Co$_{1-x}$Fe$_x$)$_2$P. (a) Co 2p, (b) Fe 2p, and (c) P 2p region. The Co 2p3/2 binding energy of np-(Co$_{1-x}$Fe$_x$)$_2$P show slightly positive shift compared with np-Co$_2$P. Moreover, the Co 2p3/2 binding energies of np-(Co$_{0.52}$Fe$_{0.48}$)$_2$P exhibit a slightly larger positive shift compared to np-(Co$_{0.47}$Fe$_{0.53}$)$_2$P and np-(Co$_{0.69}$Fe$_{0.31}$)$_2$P, sugguesting that more electron transfer occurrs in the np-(Co$_{0.52}$Fe$_{0.48}$)$_2$P.
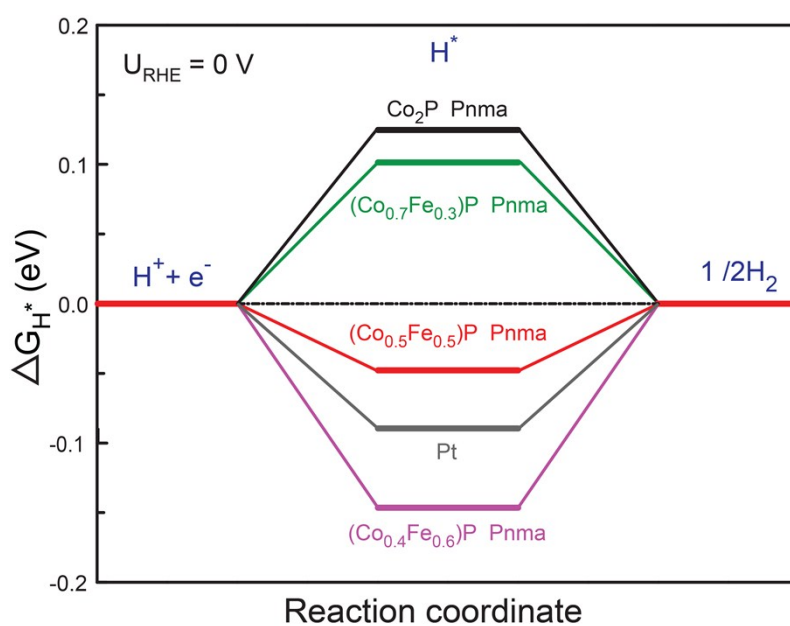

Figure S10 The DFT calculations of HER free energy diagrams at the equilibrium potential for Pt, Co$_2$P, (Co$_{0.7}$Fe$_{0.3}$)$_2$P, (Co$_{0.5}$Fe$_{0.5}$)$_2$P, and (Co$_{0.4}$Fe$_{0.6}$)$_2$P.
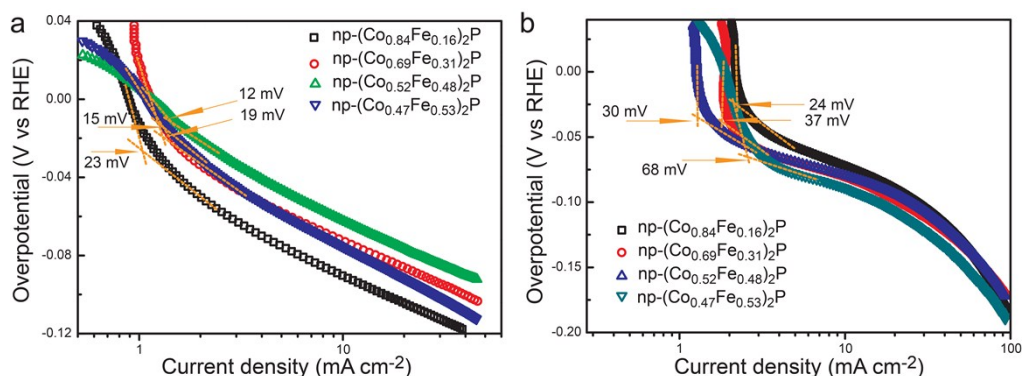
Figure S11 The onset potentials of np-$(Co_{1-x}Fe_x)_2P$ with different Co/Fe ratios in (a) 0.5 M H_2SO_4; and (b) 1.0 M KOH
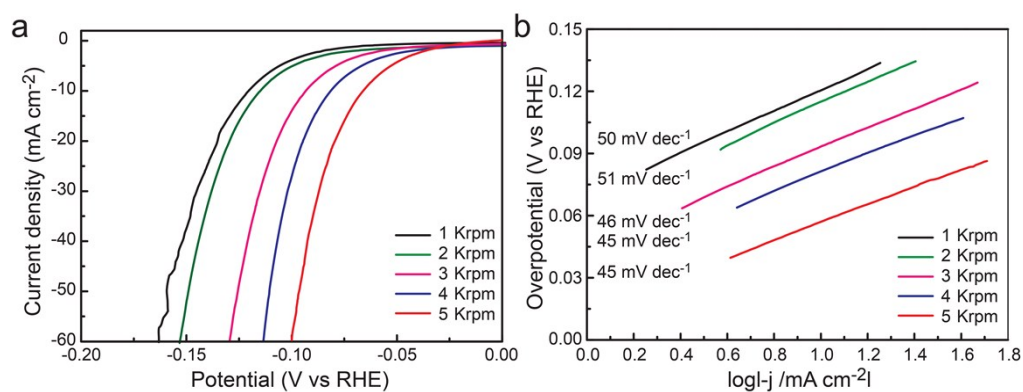
Figure S12 HER performance of np-$(Co_{0.52}Fe_{0.48})_2P$ with different pore sizes in 0.5 M H_2SO_4. **(a)** Polarization curves and **(b)** Tafel plots.
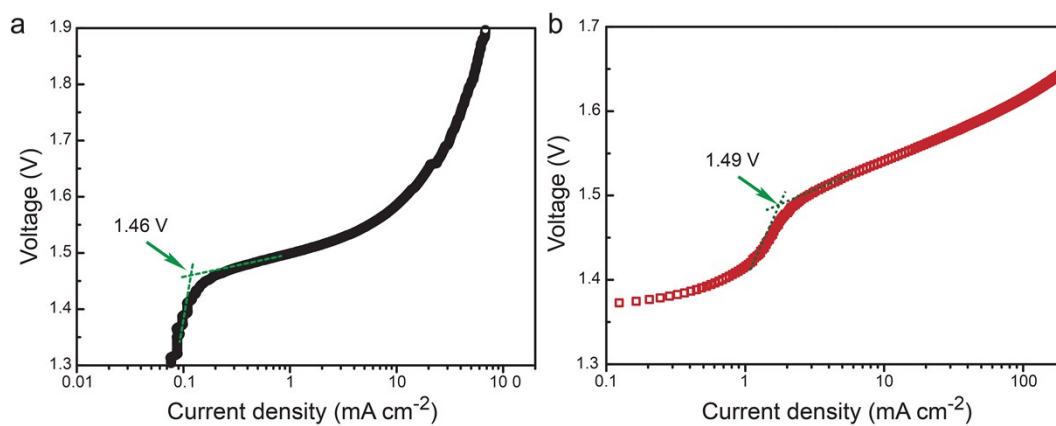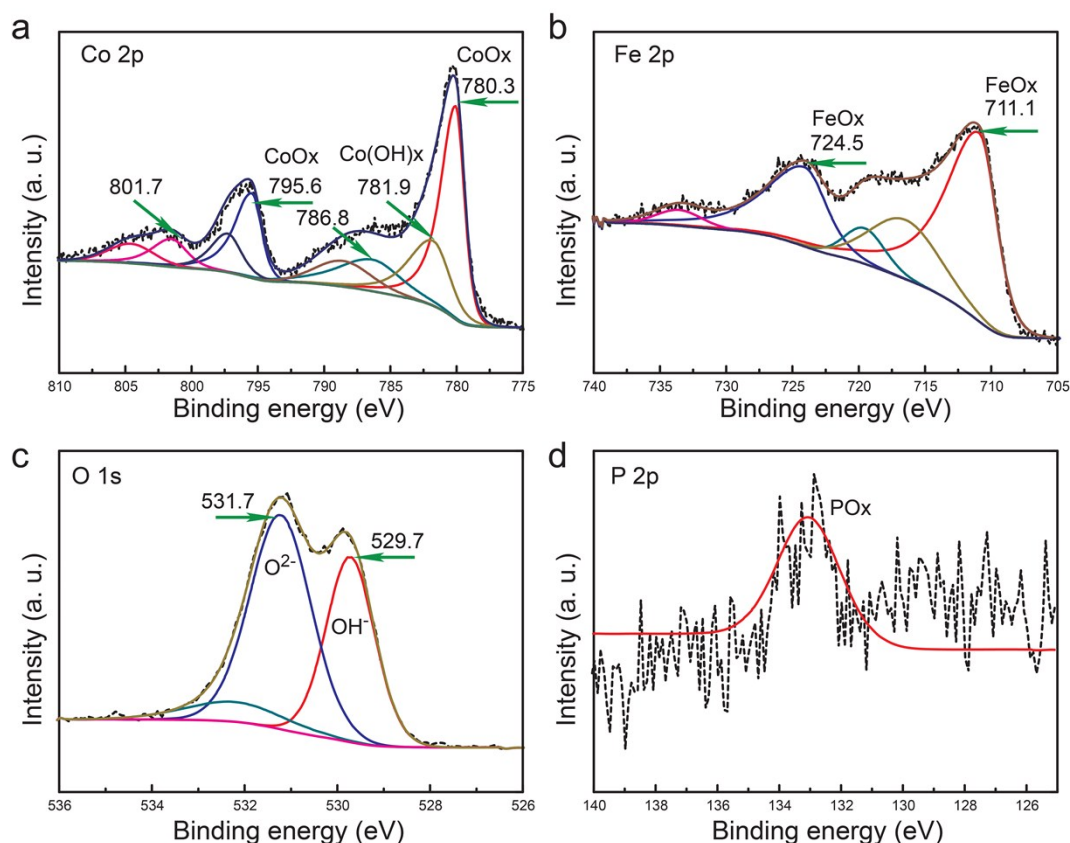
Figure S13 The onset potentials of IrO_2-Pt/C and np-$(Co_{0.52}Fe_{0.48})_2P$ electrodes for two-electrodes water splitting. (a) IrO_2-Pt/C; (b) np-$(Co_{0.52}Fe_{0.48})_2P$
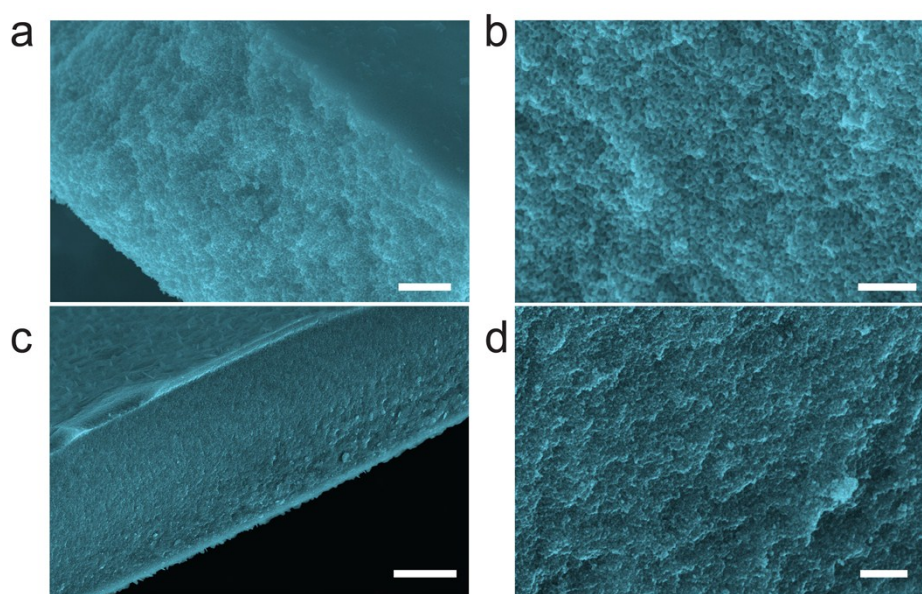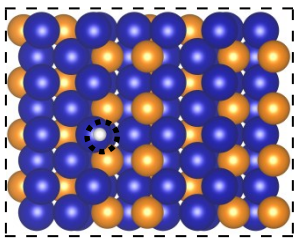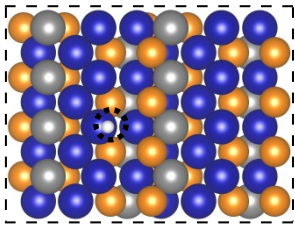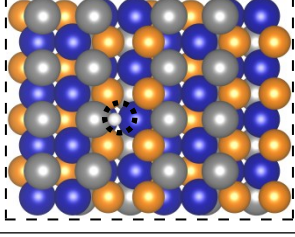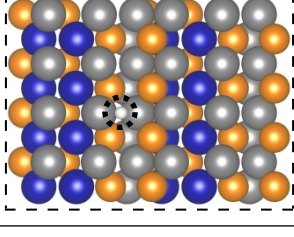

Figure S14 Cross-section SEM images of np-$(Co_{0.52}Fe_{0.48})_2P$ after long-time operation in a basic solution. (a, b) anode, (c, d) cathode. Scale bars: (a) 1 μm, (b) 500 nm, (c) 5 μm, and (d) 500 nm.

Figure S15 XPS spectra of np-(Co$_{0.52}$Fe$_{0.48}$)$_2$P after OER testing. (a) Co 2p, (b) Fe 2p, (c) O 1s, and (d) P 2p region. The Co 2p spectrum of the post-OER np-(Co$_{0.52}$Fe$_{0.48}$)$_2$P displays two peaks at 780.3 and 795.6 eV, which can be assigned to oxidized cobalt, while the peak at 781.9 is assigned to cobalt hydroxo species.[2, 3] In the spectra region of Fe 2p, the two peaks at 711.1 and 724.5 eV can be assigned to oxidized iorn. The dominant contribution at 529.7 eV corresponding to the oxygen from oxides/hydroxides appears, along with the typical surface hydroxyl species at 531.1 eV.[4] A single peak located at 133.2 eV in P 2p spectrum is ascribed to phosphate species, as well as the complete disappearance of the phosphide components around the binding energy of 129.6 eV.[5] These results indicate the reassembly of the np-(Co$_{0.52}$Fe$_{0.48}$)$_2$P surface during anodic electrochemical oxygen evolution. Therefore, the synergistic effect from the cobalt iron oxo/hydroxo species and phosphate species contributes to the improved oxygen evolution performance.

Table S1 Calculated hydrogen adsorption free energy ΔG_H. The DFT calculations were performed on different phosphide compounds according to the Ref. 1. For HER activities, the (101) surfaces are considered as the most likely active surfaces in the Pnma space group structure.

compound	space group	surface	structure	site	$\Delta G_H(eV)$
Co_2P	Pnma	(101)		Co	0.12467
$(Co_{0.7}Fe_{0.3})_2P$	Pnma	(101)		Co	0.10285
$(Co_{0.5}Fe_{0.5})_2P$	Pnma	(101)		Fe-Co-bridge	-0.0477
$(Co_{0.4}Fe_{0.6})_2P$	Pnma	(101)		Fe-bridge	-0.14798

*The adsorbed H sites in the model are highlighted by dashed circles

Table S2 HER performances of np-$(Co_{0.52}Fe_{0.48})_2P$ and other reported electrocatalysts in acidic electrolytes. (*j: current density; η: overpotential; $η_0$: onset potential)

Catalysts	Substrate	electrolyte	$η_0$ (mV)	η (mV) at j=10 mA cm^{-2}	Tafel slope (mV dec^{-1})	Reference
np-$(Co_{0.52}Fe_{0.48})_2P$	Free-standing	0.5 M H_2SO_4	12	64	45	This work
Co_2P NPs	GEC	0.5 M H_2SO_4	N/A	95	45	*Chem. Mater.* **2015**, 27, 3769
Co_2P nanorods	Ti foil	0.5 M H_2SO_4	N/A	134	71	*Nano Energy* **2014**, 9, 373
Porous Co-based film	Au film	0.5 M H_2SO_4	35	150	53	*Adv. Mater.* **2015**, 27, 3175
CoP	Ti foil	0.5 M H_2SO_4	N/A	N/A	50	*Angew. Chen.Int. Ed.* **2014**, 53, 6710
CoP	Carbon cloth	0.5 M H_2SO_4	38	75	51	*J. Am. Chem. Soc.* **2014**, 136, 7587
CoP/CNT	GEC	0.5 M H_2SO_4	40	122	54	*Angew. Chen. Int. Ed.* **2014**, 53, 5427
CoP	Ti foil	0.5 M H_2SO_4	40	90	43	*Chem. Mater.* **2014**, 26, 4326
Ni_2P NPs	GEC	0.5 M H_2SO_4	>50	117	46	*J. Am. Chem. Soc.* **2013**, 135, 9267
$Ni_{12}P_5$	Ti foil	0.5 M H_2SO_4	N/A	107	63	*Acs Nano* **2014**, 8, 8121
Cu_3P NW	CF	0.5 M H_2SO_4	62	143	67	*Angew. Chen. Int. Ed.* **2014**, 53, 9577
MoP	GCE	0.5 M H_2SO_4	40	125	54	*Adv. Mater.* **2014**, 26, 5702
Mo_2C/CNT	CP	0.1 M $HClO_4$	N/A	63	55.2	*Energ. Environ. Sci.* **2013**, 6, 943
P-WC/RGO	GCE	0.5 M H_2SO_4	46	85	54	*Angew. Chen. Int. Ed.* **2015**, 54, 6325
Porous Mo_2C	GCE	0.5 M H_2SO_4	25	142	53	*Nat. Commun.* **2015**, 6, 6512
Co-NRCNT	GCE	0.5 M H_2SO_4	50	260	69	*Angew. Chen.Int. Ed.* **2014**, 56, 4461
Double-gyroid MoS_2	FTO	0.5 M H_2SO_4	N/A	~220	50	*Nat.Mater.* **2012**, 11, 963
WS_2 nanosheets	GCE	0.5 M H_2SO_4	N/A	~240	55	*Nat.Mater.* **2013**, 12, 850

Table S3 HER performances of np-$(Co_{0.52}Fe_{0.48})_2P$ and other reported electrocatalysts in basic electrolytes (*j: current density; η: overpotential; $η_0$: onset potential).

Catalysts	Substrate	electrolyte	$η_0$ (mV)	η (mV) at j=10 mA cm^{-2}	Tafel slope (mV dec^{-1})	Reference
np-$(Co_{0.52}Fe_{0.48})_2P$	Free-standing	1.0 M KOH	30	79	40	This work
Co_2P nanorods	Ti foil	1.0 M KOH	N/A	152	N/A	*Nano Energy* **2014**, 9, 373
Porous Co-based film	Au film	1.0 M KOH	N/A	~375	N/A	*Adv. Mater.* **2015**, 27, 3175
Co-NRCNT	GCE	1.0 M KOH	N/A	370	N/A	*Angew. Chen. Int. Ed.* **2014**, 53, 4372
Ni_2P	GEC	1.0 M KOH	N/A	205	N/A	*J. Am. Chem. Soc.* **2013**, 135, 9267
CoP	CC	1.0 M KOH	N/A	209	129	*J. Am. Chem. Soc.* **2014**, 136, 7587
FeP NAs NW	CC	1.0 M KOH	N/A	218	146	*ACS Catal.* **2014**, 4 4065
MoB	GCE	0.1 M KOH	N/A	225	59	*Angew. Chen. Int. Ed.* **2012**, 51, 12703
Porous Mo_2C	GCE	1.0 M KOH	80	151	59	*Nat. Commun.* **2015**, 6, 6512
$Ni/Ni(OH)_2$	GCE	0.1M KOH	N/A	300	128	*Angew. Chen. Int. Ed.* **2012**, 51, 12495
Ni/NiO/CNT	GCE	1.0 M KOH	N/A	80	82	*Nat. Commun.* **2014**, 4, 4695
Co/Co_3O_4	Ni foam	1.0 M KOH	30	90	44	*Nano.Lett.* **2015**, 15, 6015.
WC	Ni foam	0.1M KOH	N/A	220	N/A	*J. Am. Chem. Soc.* **2015**, 137, 5480

Table S4 Comparison of reported nonprecious metal electrocatalysts for OER in basic electrolytes. (j: current density; η: overpotential)

Catalysts	Substrate	electrolyte	η (mV) at j=10 mA cm^{-2}	Tafel slope (mV dec^{-1})	Reference
np-$(Co_{0.52}Fe_{0.48})_2P$	Free-standing	1.0 M KOH	270	30	This work
Co-P film	Co foil	1.0 M KOH	345	47	*Angew. Chen. Int. Ed.* **2015**, 54, 6251
NiCo LHD	GCE	1.0 M KOH	367	40	*Nano. Lett.* **2015**,15, 1421
CoCo LHD	GEC	1.0 M KOH	393	59	*Nat.Commun.* **2014**, 5, 4477
NiFeO$_x$ film	CC	1.0 M KOH	>350	N/A	*J. Am. Chem. Soc.* **2013**, 135, 16977
MnO$_2$ film	CC	1.0 M KOH	563	49	*J. Am. Chem. Soc.* **2013**, 134, 17253
CoO NG	GCE	0.1 M KOH	340	71	*Energy Environ. Sci.* **2014**,7,609
Co$_x$O$_y$/NC	GCE	0.1 M KOH	430	N/A	*Angew. Chen. Int. Ed.* **2014**, 53, 8508
Ni$_x$Co$_{3-x}$O$_4$ nanowire	GCE	1.0 M KOH	370	59-64	*Adv. Mater.* **2010**, 22, 1924
De-LiCoO$_2$	GCE	0.1 M KOH	400	50	*Nat. Commun.* **2014**, 5, 4345
CoMn LDH	GCE	1.0 M KOH	324	43	*J. Am. Chem. Soc.* **2014**, 136, 16481
CO$_3$O$_4$/rm-GO	Ni foam	1.0 M KOH	310	67	*Nat. Mater,* **2011**,10,780
CoO$_x$ film	Ni foam	1.0 KOH	403	42	*J. Am. Chem. Soc.* **2012**, 134, 17253

Table S5 Bifunctional electrocatalyst for overall water splitting in 1.0 M KOH solution. (j: current density; η: overpotential)

Catalysts (Cathode (H_2))	Catalysts (anode (O_2))	Substrate	η at j=10 mA cm^{-2} (V)	Reference
np-$(Co_{0.52}Fe_{0.48})_2P$	np-$(Co_{0.52}Fe_{0.48})_2P$	Free-standing	1.53	This works
NiFe LDH	NiFe LDH	Ni foam	~1.70	*Science* **2014**, 345, 1593
CoO_x/NC	CoO_x/NC	Ni foam	1.62	*J. Am. Chem. Soc.* **2015**, 137, 2688
NiSe NWs	NiSe NWS	Ni foam	1.63	*Angew. Chen. Int. Ed.* **2015**, 54, 9351
Ni-Fe-O	Ni-Fe-O	Ni foam	1.51	*Nat. Commun.* **2015**, 6, 7261
$Ni_{0.33}Co_{0.67}S_2$	$NiCoO_4$	Ti foil	~1.73	*Adv. Energy Mater.* **2015**, 5, 1402031
Ni_2P nanoparticle	Ni_2P nanoparticle	Ni foam	1.63	*Energy Environ. Sci.* **2015**, 8, 2347
Ni_4P_5 film	Ni_4P_5 film	Ni film	1.7	*Angew. Chem. Int. Ed.* **2015,** 54, 12361.
Co-P film	Co-P film	Co foil	1.63	*Angew. Chen. Int. Ed.* **2015**, 54, 6251
EG/$Co_{0.85}$Se/NiFe-LDH	EG/$Co_{0.85}$Se/NiFe-LDH	EG foil	1.67	*Energy Environ. Sci.* **2016**, 9, 478
CoP nanorod	CoP nanorod	Ni foam	1.62	*Adv. Funct. Mater.* **2015**, 25, 7337
CP/CTs/Co-S	CP/CTs/Co-S	CP	1.743	*Acs Nano* **2016**, 10, 2342
ONPPGC/OCC	ONPPGC/OCC	CC	1.66	*Energy Environ. Sci.* **2016**, **9**, 1210

References

1. J. Kibsgaard, C. Tsai, K. Chan, J. D. Benck, J. K. Norskov, F. Abild-Pedersen and T. F. Jaramillo, *Energ. Environ. Sci.*, 2015, **8**, 3022-3029.
2. J. Yang, H. Liu, W. N. Martens and R. L. Frost, *J. Phys.Chem. C*, 2010, **114**, 111-119.
3. F. H. Saadi, A. I. Carim, E. Verlage, J. C. Hemminger, N. S. Lewis and M. P. Soriaga, . *J. Phys.Chem. C*, 2014, **118**, 29294–29300.
4. M. C. Biesinger, B. P. Payne, A. P. Grosvenor, L. W. M. Lau, A. R. Gerson and R. S. C. Smart, *Appl. Surf. Sci.*, 2011, **257**, 2717-2730.
5. N. Jiang, B. You, M. Sheng and Y. Sun, *Angew. Chem. Int. Ed.*, 2015, **54**,

6251-6254.